Experimental Probing of Canonical Electromagnetic Spin Angular Momentum Distribution via Valley-Polarized Photoluminescence

Donghyeong Kim and Min-Kyo Seo*
Department of Physics, Korea Advanced Institute of Science and Technology, Daejeon 34141, Korea

(Received 28 July 2021; accepted 28 October 2021; published 24 November 2021)

The canonical formulation of the spin angular momentum (SAM) of light has been suggested recently as an extension of the Abraham-Minkowski controversy. However, experimental substantiations of the canonical SAM for localized fields have not been reported yet. We directly probe the locally distributed canonical SAM tailored by a plasmonic nanostructure via the valley-polarized photoluminescence of the multilayer WS_2. The spectrum-resolved measurement details the spin-selective Raman scattering and exciton emission beyond the conventional manner of employing circularly polarized paraxial waves.

DOI: 10.1103/PhysRevLett.127.223601

Light carries both orbital and spin angular momenta. In the paraxial limit, the helical spatial distribution of the wavefront and the degree of circular polarization (DoCP) correspond to the orbital and spin parts of the classical angular momentum of light, respectively [1–3]. The spin angular momentum (SAM) of light plays a crucial role in various light–matter interactions and their application. The selection rules of electromagnetic transitions in atoms, molecules, and condensed matter feature the conservation of the total angular momentum, including the optical SAM [4–6]. Molecular chirality [7] and magneto-optic effects [8,9] are inevitably related to the SAM of light. The circularly polarized light beam can cause mechanical spinning motion of an object [10]. Thus, it is essential to understand the electromagnetic SAM and how it transfers to its electronic, magnetic, molecular, or mechanical counterparts. Moreover, a number of interesting studies have been conducted based on the interaction between the SAM of light and the nanophotonic platform [11–15]. The optical analog of the spin Hall effect [16–18] and manipulation of electromagnetic waves [19–21] have been reported recently.

The typical representation of the angular momentum of the electromagnetic fields propagating paraxially in the free space $(\mathbf{J}_{\mathrm{typ}} = \varepsilon_0 \int \mathbf{x} \times (\mathbf{E} \times \mathbf{B}) d^3\mathbf{x} = \varepsilon_0 \int (\mathbf{E} \times \mathbf{B}) d^3\mathbf{x} + \varepsilon_0 \int \sum_{i=1}^{3} E_i (\mathbf{x} \times \nabla) A_i d^3\mathbf{x} = \mathbf{S}_{\mathrm{typ}} + \mathbf{L}_{\mathrm{typ}})$ allows us to distinguish the orbital and spin components, considering the analog to the quantum mechanical orbital angular momentum operator. However, the integral evaluation of the total angular momentum, depending on the choice of the origin of the coordinates, is inherently incapable of considering the spatial distribution and density of the electromagnetic angular momentum, particularly in the presence of matter [22,23]. In addition, except for the case of free-propagating paraxial waves, both the integrated orbital and spin angular momenta do not obey the well-known commutation rule in the analog to the quantum mechanical operators [24]. The discussion on electromagnetic momentum, both linear and angular, has a long history, the so-called Abraham-Minkowski controversy [25,26]. Recently, the concept of the canonical angular momentum, an alternative to the typical representation, has been suggested, accompanied by theoretical self-consistency [26–28]. The canonical form of the angular momentum of light, derived from the introduction of the dual symmetry to the electromagnetic field tensor, is free from the issues of the typical representation that cannot determine the SAM for structured or localized light or address the intrinsic distinguishment of the optical angular and spin momentum.

However, direct and experimental probing of the canonical angular momentum and its local distribution that an optical nanostructure is ready to create has not been demonstrated thus far. Only a few reports have examined the validity of the canonical angular momentum limited to light propagating in the free space or existing in the interface between two homogeneous dielectric media [29]. Recently, two-dimensional transition metal dichalcogenides have been found to have the possibility of featuring the SAM carried by not only the free-propagating circularly polarized light [6,30–32] but also the optical modes of nanophotonic waveguides and metamaterials [33–35] in their photoluminescence (PL), based on valley-selective excitation and valley-polarized emission. In this study, we have experimentally demonstrated that the valley-polarized PL of the multilayer WS_2 can directly probe and image the canonical SAM distribution carried by a structured, localized electromagnetic field. We employed a plasmonic-connected V-shaped gold nanostructure array that provided the local field distribution, tailored to the wavelength scale with linearly polarized incident light. The spectrum-resolved measurement informs us of the interaction properties of the Raman scattering and exciton emission with the

canonical SAM. Further, we addressed the SAM per unit electromagnetic field energy to quantify the probability that a single photon takes the positive or negative spin with respect to the normal of the multilayer WS_2 plane.

The canonical SAM density is determined as follows:

$$\mathbf{S}_{\mathrm{can}} = \frac{1}{4\pi}\mathrm{Im}[\varepsilon\mathbf{E}^* \times \mathbf{E} + \mu\mathbf{H}^* \times \mathbf{H}]. \quad (1)$$

As illustrated in Fig. 1(a), an optical nanostructure induces and distributes the canonical SAM density of light around its territory. Even for the incidence of the linearly polarized light that, by itself, does not carry any canonical angular momentum, the optical nanostructure that provides a phase difference between the orthogonal components of the induced fields results in a localized, nonzero SAM. The geometric configuration and material composition (metals or dielectrics) of the optical nanostructure determined the direction and strength of the canonical SAM density vector, depending upon the position. The multilayer WS_2 flake acts as a probe for the local density of the canonical SAM. Conventionally, valley-selective excitation and valley-polarized emission caused by the broken symmetry between the K and K' valleys lead to valley-polarized PL, under the excitation of circularly polarized light. In this study, we realized the ability of valley-polarized PL to probe the vertical component of the locally distributed canonical SAM induced by the optical nanostructure of interest.

We examined the valley-polarized PL of the employed multilayer WS_2 flake at room temperature under resonant excitation of left-handed circularly polarized light [Fig. 1(b)]. The degree of valley polarization of the PL from multilayer WS_2 flakes has been reported to be higher than 0.7 at room temperature [36–38]. Meanwhile, the PL of the monolayer WS_2 exhibits a valley polarization degree of only ~0.5, even at the cryostat temperature, owing to the significant intervalley scattering [37,39]. Based on a scanning confocal microscope setup with a 594-nm-wavelength laser incident from the substrate side (see Fig. S1 in the Supplemental Material [40]), we verified that the selected multilayer WS_2 flake supports PL with a high degree of valley polarization, which is up to ~0.81 at the peak wavelength of the exciton emission (i.e., 620 nm). We scanned and evaluated the total intensity of the valley-polarized PL depending on the position [Figs. 1(c) and 1(d)]. The average degree of valley polarization of the total PL is ~0.51 over the area (black rectangle) where the plasmonic nanostructure array will be located, supporting an excellent spatial uniformity with a standard deviation of only ~0.061 appropriate for measuring the canonical SAM distribution.

Plasmonic nanostructures provide an excellent test platform to create and probe a locally distributed canonical SAM. In this study, we employed a connected V-shaped gold nanostructure and its array. Figure 2(a) shows the spatial distribution of the calculated canonical SAM density in a single unit cell, including the connected V-shaped gold nanostructure. Two gold rods with the length and width of 760 and 80 nm, respectively, were connected at a right angle. The upper and lower rods generate surface plasmon polariton fields supporting the canonical SAM of the positive $(+z)$ and negative $(-z)$ vertical components, respectively, under the illumination of an incident light linearly polarized along the y axis. Figure 2(b) shows the canonical SAM density distribution over the array (left) and its expected distribution considering the blurring effect of the employed objective lens realized by the convolution with the Airy function of the full width at half maximum of 330 nm (right). According to the periodic arrangement of the unit cells, the stripes of the positive and negative canonical SAM appear repeatedly. As shown in Figs. 2(c)

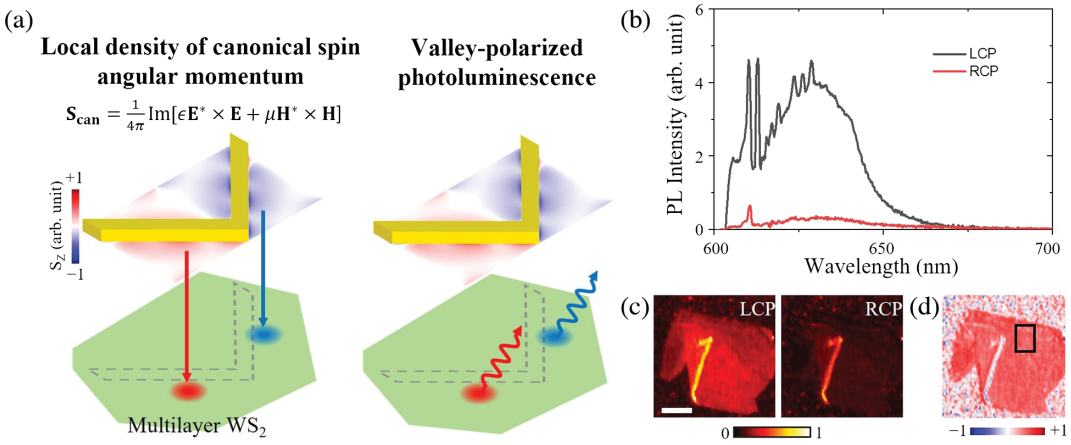

FIG. 1. (a) Schematic of the local distribution of the canonical SAM generated by an optical nanostructure and probed by the valley-polarized PL of the multilayer WS_2. (b) Typical valley-polarized PL spectrum of the employed multilayer WS_2 flake under the planewave 594-nm-laser excitation of the left-handed circular polarization. In the spectrum, the DoCP of the A exciton emission is ~0.83. (c,d) Measured distributions of the left- and right-handed circularly polarized PL (c) and the DoCP (d) over the multilayer WS_2 flake under the left-handed circularly polarized excitation. Scale bar, 10 μm.

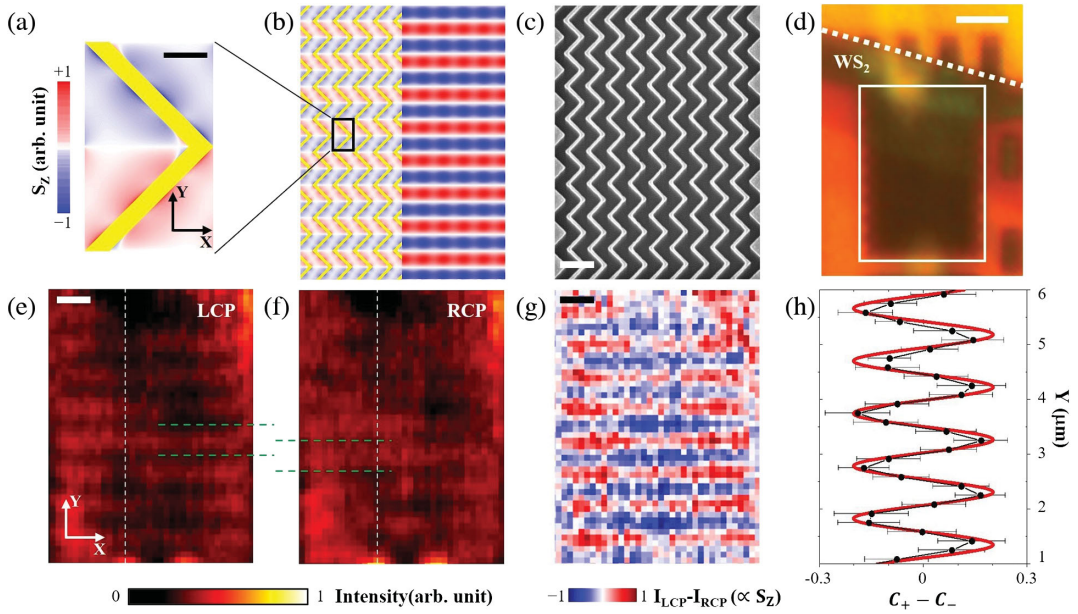

FIG. 2. (a) Calculated distribution of the vertical component (S_z) of the canonical SAM density generated by the connected V-shape gold structure under the planewave incidence, linearly polarized along the y axis; scale bar, 200 nm. (b) Calculated canonical SAM distribution over the nanostructure array (left) and expected valley-polarized PL distribution considering the diffraction by the objective lens (right). (c) Scanning electron microscope image of the fabricated connected V-shape gold nanostructure array; scale bar, 1 μm. (d) Optical microscope image of the measured sample. The V-shape gold nanostructure array (the white box) entirely overlays the multilayer WS_2 flake (the area below the white dashed line); scale bar, 2.5 μm. (e),(f) Measured PL intensity distributions with the left- (e) and right-handed (f) circular polarization states. The step size of scanning is 166.7 nm. The green dashed lines guide the positions of the nodes of PL for comparison; scale bar, 1 μm. (g) Measured canonical SAM distribution; scale bar, 1 μm. (h) Measured (black) and calculated (red) $C_+ - C_-$ depending on the position along the y axis.

and 2(d), we fabricated the array of connected V-shaped gold nanostructures in a 50-nm-thick gold film, and then we placed it onto the selected multilayer WS_2 flake on the glass substrate (see Fig. S2 in Supplemental Material [40]). The multilayer WS_2 flake in Fig. 2(d) is identical to that shown in Figs. 1(c) and 1(d).

Figures 2(e) and 2(f) show the measured intensity distributions of PL in the left- and right-handed circular polarization states, respectively. Coupled with the plasmonic V-shaped gold nanostructure array, the electromagnetic field of the 594-nm-wavelength incident laser generated a spatially inhomogeneous distribution of the canonical SAM, which was probed in terms of the DoCP of the valley-polarized PL of the multilayer WS_2 flake. The PL signals were also collected by the objective lens at the substrate side and coupled with an optical fiber connected to a single-photon avalanche photodiode. We note that the collection efficiency of the PL at the glass ($n = 1.414$) substrate side is significantly higher than that in the air ($n = 1$) superstrate. The PL in the left- and right-handed circular polarization from the point of view of the observer in the substrate side corresponds to the probing of the positive and negative canonical SAM, respectively. The repeating stripe pattern of PL appeared in agreement with the theoretical prediction, and the intensity maxima related to the positive and negative SAM alternated exactly with each other.

The difference between the left- and right-handed circularly polarized PL intensity distributions corresponds to the spatial distribution of the vertical component of the canonical SAM density, as shown in Fig. 2(g). In agreement with the simulated expectation in Fig. 2(b), the multilayer WS_2 successfully probed the canonical SAM distribution on the plasmonic nanostructure as it is. The DoCP of the measured PL provides information on the canonical SAM per unit energy, which ultimately describes the probability that the vertical component of the canonical SAM of a single photon or polariton will be measured as positive or negative. Retaining the degree of valley polarization (η) of the PL of the multilayer WS_2 flake, we used the following equations to connect the measured intensities of the left- and right-handed circularly polarized PL (I^m_{LCP} and I^m_{RCP}) and the probabilities of the positive and negative canonical SAM (C_+ and C_-).

$$\begin{bmatrix} I^m_{\mathrm{LCP}} \\ I^m_{\mathrm{RCP}} \end{bmatrix} \propto \begin{bmatrix} \frac{1+\eta}{2} & \frac{1-\eta}{2} \\ \frac{1-\eta}{2} & \frac{1+\eta}{2} \end{bmatrix} \begin{bmatrix} C_+ \\ C_- \end{bmatrix}, \tag{2}$$

$$\frac{C_+ - C_-}{C_+ + C_-} = \frac{I^m_{\mathrm{LCP}} - I^m_{\mathrm{RCP}}}{\eta I^m_{\mathrm{LCP}} + \eta I^m_{\mathrm{RCP}}} = \frac{1}{\eta}\frac{I^m_{\mathrm{LCP}} - I^m_{\mathrm{RCP}}}{I^m_{\mathrm{LCP}} + I^m_{\mathrm{RCP}}} = \frac{1}{\eta}\mathrm{DoCP}. \tag{3}$$

Figure 2(h) shows the probability difference extracted from the measured DoCP depending on its position along the y axis. The black curve and the error bar are the mean and standard deviation of the measured data, respectively, obtained over 6 μm along the x axis for the given y position. Here, we employed the degree of valley polarization (i.e., 0.51), as measured in Fig. 1(d). The condition $C_+ + C_- = 1$ provided the probability of each positive and negative vertical projection of the SAM. The obtained $C_+ - C_-$ of ~0.19 corresponds to the probability of ~0.595 (~0.405) that a photon or polariton takes the positive (negative) vertical component of the SAM. The solid red curve is the simulated canonical SAM density, normalized by the energy density of the in-plane electromagnetic field components divided by its angular frequency [28]. This unitless quantity corresponds to the expectation value of the probability of the vertical component of the SAM, $(C_+ - C_-)/(C_+ + C_-)$. The simulated result excellently meets the mean of the experimental measurement within 1 standard deviation. We note that the carrier doping possible to occur very near the metal-WS_2 interface might affect the local valley polarization, but its effect on the results and analyses of the vertical component of the canonical SAM density distribution in the employed plasmonic structure is insignificant (see Fig. S3 in the Supplemental Material [40]).

The spectrum-resolved measurement provides further information on how different emission processes contributing to the total PL, such as Raman scattering and exciton emission, with the canonical SAM. Figures 3(a) and 3(b) show the PL spectra of the left- and right-handed circular polarization states, respectively, depending on the position along the white dashed lines in Figs. 2(e) and 2(f). We also plotted the typical PL spectra of the left-handed circular polarization at the positions of the positive and negative canonical SAMs, respectively [Fig. 3(c)]. The PL of the multilayer WS_2 flake consists of two Raman scattering peaks (i.e., the well-known E^1_{2g} and A_{1g} modes) and wideband A exciton emission [41,42]. The E^1_{2g}- and A_{1g} -mode Raman scattering peaks are at the wavelengths of 606.3 (341.5) and 608.8 nm (409.3 cm^{-1}), respectively. The A exciton emission with a broad spectral distribution around 620 nm dominated the total PL intensity in Fig. 2(g), compared to the Raman scattering emissions of sharp spectral peaks.

To visualize the dependency of the two Raman scattering and exciton emissions on the canonical SAM, we plotted the intensities of the three spectral peaks depending on the position along the y axis [Fig. 3(d)]. Notably, the E^1_{2g}-mode Raman scattering exhibits opposite behavior to that of the A exciton emission. The cross-polarized emission behavior in terms of the SAM indicates that the off-diagonal terms dominate in the Raman scattering tensor [43]. On the other hand, the A_{1g}-mode Raman scattering did not show a clear polarization dependence as compared to the others. It has been reported that the Raman scattering modes in the WS_2 mono- or multilayer can be co-polarized or cross polarized

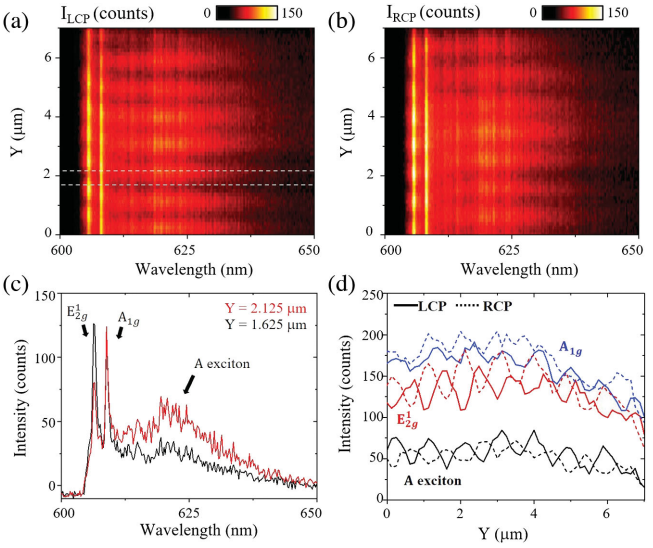

FIG. 3. (a),(b) Measured PL spectra of the left- (a) and right-handed (b) circular polarization depending on the position along the white dashed lines in Figs. 2(e) and 2(f), respectively. (c) PL spectra at two different y positions indicated by the white dashed lines in (a). (d) The stack plot of the PL intensities of the A exciton and Raman scattering of the A_{1g} and E^1_{2g} modes depending on the position along the y axis as the canonical SAM essentially changes. Stack offset is 30 counts.

depending on the intrinsic doping level, operating temperature, and excitation condition [44–47]. We expect that the use of Raman scattering peaks will allow measurements of a variety of wavelengths, depending on the choice of the excitation laser. In addition, tailored local canonical SAM distribution in a structured nanophotonic bath results in the rise to the engineering of spin-selective or polarized transitions beyond the conventional manners of employing circularly polarized paraxial waves.

To substantiate the results of probing the canonical SAM density and its local distribution, we conducted a control experiment in which the WS_2 multilayer was replaced with a thin layer of dye molecules without a spin-selective excitation or spin-polarized PL character as shown in Fig. 4(a). We employed the Texas Red dye molecule with the excitation and emission spectra maximized at wavelengths of ~595 and ~620 nm, respectively, which well matched the wavelengths of the resonant excitation and exciton emission of the WS_2 multilayer. The control experiment examines whether the PL from the emitter, coupled to the employed plasmonic nanostructure, is accompanied by an artificial change or perturbation in the DoCP. By removing the probability of artificial polarization state changes, we verified the role of the valley-polarized PL of the WS_2 multilayer, as a probe of the canonical SAM density. Figures 4(b) and 4(c) show the measured intensity distributions of PL in the left- and right-handed circular polarization states, respectively. Any spatial change in the polarization-resolved PL intensity associated with the canonical SAM distribution was not

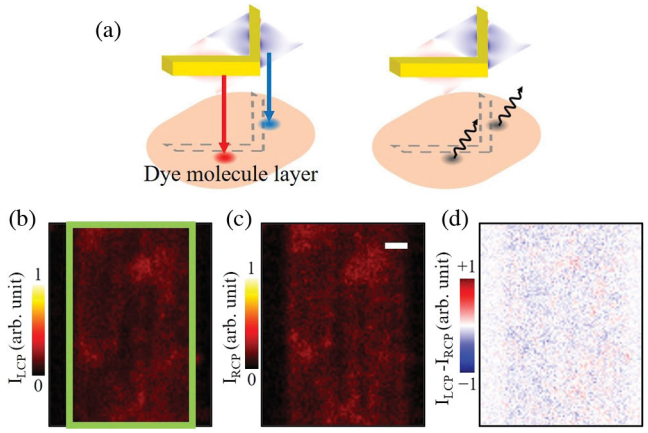

FIG. 4. (a) Schematic of the response of the dye molecule layer (Texas red dye molecule) that washes out the canonical SAM distribution. (b),(c) Measured PL intensity distributions with the left- (b) and right-handed (c) circular polarization states; scale bar, 1 μm. The green box indicates the area of the connected V-shape gold nanostructure array. (d). Difference between the PL intensity measured in (b) and (c).

observed. Only a few vertical stripes along the alignment direction of the connected V-shaped gold nanostructures were observable. The measured PL distributions in the left- and right-handed circular polarization states were almost identical; their differences did not show any significant features [Fig. 4(d)].

In summary, we experimentally demonstrated probing of the canonical electromagnetic SAM by employing the valley-polarized PL of the multilayer WS_2. The plasmonic connected V-shaped nanostructure distributes the canonical SAM at the wavelength scale under linearly polarized excitation. The high uniformity of the valley-polarized PL of the employed multilayer WS_2 flake allows high-quality imaging of the canonical SAM distribution. The control experiment employing the thin layer of dye molecules with spin-independent PL solidifies the capability of the multilayer WS_2 to truly probe the canonical SAM. The DoCP of the measured PL enables us to quantitatively examine the SAM per unit of electromagnetic energy. We expect that the rigorous consideration of the canonical SAM will become increasingly important in various investigations and applications dealing with spin-selective transitions from an electromagnetic field to electronic or mechanical entities and vice versa.

M.-K. S. acknowledges support by KAIST Cross-Generation Collaborative Lab project and the National Research Foundation of Korea (NRF) (2020R1A2C2014685, 2020R1A4A2002828).

*Corresponding author.
minkyo_seo@kaist.ac.kr

[1] J. D. Jackson, *Classical Electrodynamics* (Wiley, New York, 1975).
[2] L. Allen, S. Barnett, and M. Padgett, *Optical Angular Momentum* (Institute of Physics Publishing, Bristol, United Kingdom, 2003).
[3] D. L. Andrews and M. Babiker, *The Angular Momentum of Light* (Cambridge University Press, Cambridge, England, 2012).
[4] C. Cohen-Tannoudji, B. Diu, and F. Laloë, *Quantum Mechanics* (Wiley-VCH, New York, 1992).
[5] T. P. Softley, *Atomic Spectra* (Oxford University Press, New York, 1994).
[6] T. Cao, G. Wang, W. Han, H. Ye, C. Zhu, J. Shi, Q. Niu, P. Tan, E. Wang, B. Liu, and J. Feng, Nat. Commun. **3**, 887 (2012).
[7] P. Atkins and J. d. Paula, *Elements of Physical Chemistry*, 6th ed. (Oxford University Press, New York, 2015).
[8] R. Schafer and A. Hubert, *Magnetic Domains: The Analysis of Magnetic* (Springer, New York, 1998).
[9] D. Kim, Y.-W. Oh, J. U. Kim, S. Lee, A. Baucour, J. Shin, K.-J. Kim, B.-G. Park, and M.-K. Seo, Nat. Commun. **11**, 5937 (2020).
[10] Y. Zhao, D. Shapiro, D. Mcgloin, D. T. Chiu, and S. Marchesini, Opt. Express **17**, 23316 (2009).
[11] M. D. Turner, M. Saba, Q. Zhang, B. P. Cumming, G. E. Schröder-Turk, and M. Gu, Nat. Photonics **7**, 801 (2013).
[12] N. Shitrit, I. Yulevich, E. Maguid, D. Ozeri, D. Veksler, V. Kleiner, and E. Hasman, Science **340**, 724 (2013).
[13] G. Spektor, A. David, B. Gjonaj, G. Bartal, and M. Orenstein, Nano Lett. **15**, 5739 (2015).
[14] Y. Huang, V. Polojärvi, S. Hiura, P. Höjer, A. Aho, R. Isoaho, T. Hakkarainen, M. Guina, S. Sato, J. Takayama, A. Murayama, I. A. Buyanova, and W. M. Chen, Nat. Photonics **15**, 475 (2021).
[15] S. Kim, Y.-C. Lim, R. M. Kim, J. E. Fröch, T. N. Tran, K. T. Nam, and I. Aharonovich, Small **16**, 2003005 (2020).
[16] A. Kavokin, G. Malpuech, and M. Glazov, Phys. Rev. Lett. **95**, 136601 (2005).
[17] C. Leyder, M. Romanelli, E. G. J. Ph. Karr, T. C. H. Liew, M. M. Glazov, A. V. Kavokin, G. Malpuech, and A. Bramati, Nat. Phys. **3**, 628 (2007).
[18] K. Y. Bliokh, D. Smirnova, and F. Nori, Science **348**, 1448 (2015).
[19] J. Petersen, J. Volz, and A. Rauschenbeutel, Science **346**, 67 (2014).
[20] L. Huang, X. Chen, H. Mühlenbernd, G. Li, B. Bai, Q. Tan, G. Jin, T. Zentgraf, and A. S. Zhang, Nano Lett. **12**, 5750 (2012).
[21] G. Zheng, H. Mühlenbernd, M. Kenney, G. Li, T. Zentgraf, and S. Zhang, Nat. Nanotechnol. **10**, 308 (2015).
[22] I. Bialynicki-Birula andZ. Bialynicka-Birula, J. Opt. **13**, 064014 (2011).
[23] C.-F. Li, Phys. Rev. A **80**, 063814 (2009).
[24] S. V. Enk and G. Nienhuis, J. Mod. Opt. **41**, 963 (1994).
[25] U. Leonhardt, Nature (London) **444**, 823 (2006).
[26] K. Y. Bliokh, A. Y. Bekshaev, and F. Nori, New J. Phys. **19**, 123014 (2017).
[27] K. Y. Bliokh, A. Y. Bekshaev, and F. Nori, New J. Phys. **15**, 033026 (2013).
[28] K. Y. Bliokh, A. Y. Bekshaev, and F. Nori, Phys. Rev. Lett. **119**, 073901 (2017).

[29] J. S. Eismann, L. H. Nicholls, D. J. Roth, M. A. Alonso, P. Banzer, F. J. Rodríguez-Fortuño, A. V. Zayats, F. Nori, and K. Y. Bliokh, Nat. Photonics **15**, 156 (2021).
[30] K. F. Mak, K. He, J. Shan, and T. F. Heinz, Nat. Nanotechnol. **7**, 494 (2012).
[31] H. Zeng, J. Dai, W. Yao, D. Xiao, and X. Cui, Nat. Nanotechnol. **7**, 490 (2012).
[32] Z. Huang, Y. Liu, K. Dini, Q. Tan, Z. Liu, H. Fang, J. Liu, T. Liew, and W. Gao, Nano Lett. **20**, 1345 (2020).
[33] S.-H. Gong, F. Alpeggiani, B. Sciacca, E. C. Garnett, and L. Kuipers, Science **359**, 443 (2018).
[34] S.-H. Gong, I. Komen, F. Alpeggiani, and L. Kuipers, Nano Lett. **20**, 4410 (2020).
[35] L. Sun, C.-Y. Wang, A. Krasnok, J. Cho, J. Shi, J. S. Gomez-Diaz, A. Zepeda, S. Gwo, C.-K. Shih, A. Alù, and X. Li, Nat. Photonics **13**, 180 (2019).
[36] B. Zhua, H. Zengb, J. Daic, Z. Gonga, and X. Cui, Proc. Natl. Acad. Sci. U.S.A. **111**, 11606 (2014).
[37] H. Su, C. Wei, A. Deng, D. Deng, C. Yangc, and J.-F. Dai, Nanoscale **9**, 5148 (2017).
[38] P. K. Nayak, F.-C. Lin, C.-H. Yeh, J.-S. Huang, and P.-W. Chiu, Nanoscale **8**, 6035 (2016).
[39] A. Hanbicki, G. Kioseoglou, M. Currie, C. S. Hellberg, K. McCreary, A. Friedman, and B. Jonker, Sci. Rep. **6**, 18885 (2016).
[40] See Supplemental Material at http://link.aps.org/supplemental/10.1103/PhysRevLett.127.223601 for more technical details.
[41] B. Zhu, X. Chen, and X. Cui, Sci. Rep. **5**, 9218 (2015).
[42] F. Wang, I. A. Kinloch, D. Wolverson, R. Tenne, A. Zak, E. O'Connell, U. Bangert, and R. J. Young, 2D Mater. **4**, 015007 (2017).
[43] A. Cantarero, C. Trallero-Giner, and M. Cardona, Phys. Rev. B **40**, 12290 (1989).
[44] S.-Y. Chen, C. Zheng, M. S. Fuhrer, and J. Yan, Nano Lett. **15**, 2526 (2015).
[45] B. Miller, J. Lindlau, M. Bommert, A. Neumann, H. Yamaguchi, A. Holleitner, A. Högele, and U. Wurstbauer, Nat. Commun. **10**, 807 (2019).
[46] X. Liu, J. Yi, S. Yang, E.-C. Lin, Y.-J. Zhang, P. Zhang, J.-F. Li, Y. Wang, Y.-H. Lee, Z.-Q. Tian, and X. Zhang, Nat. Mater. **20**, 1210 (2021).
[47] Y. Zhao, S. Han, J. Zhang, and L. Tong, J. Raman Spectrosc. **52**, 525 (2021).